Received: 26 November 2019 | Revised: 7 January 2020 | Accepted: 13 January 2020

DOI: 10.1002/eom2.12017

EcoMat FUNCTIONAL MATERIALS FOR GREEN ENERGY AND ENVIRONMENT WILEY

RESEARCH ARTICLE

Ag/In lead-free double perovskites

Fang Liu[1] | Daniela Marongiu[1] | Riccardo Pau[1] | Valerio Sarritzu[1] | Qingqian Wang[1] | Stefano Lai[1] | Alessandra G. Lehmann[1] | Francesco Quochi[1] | Michele Saba[1] | Andrea Mura[1] | Giovanni Bongiovanni[1] | Alessandro Mattoni[2] | Claudia Caddeo[2] | Andrea Bosin[1] | Alessio Filippetti[1,2]

[1]Dipartimento di Fisica, Università degli Studi di Cagliari, Monserrato, Italy

[2]Istituto Officina dei Materiali (CNR - IOM) Cagliari, Cittadella Universitaria, Monserrato, Italy

Correspondence
Michele Saba and Alessio Filippetti, Dipartimento di Fisica, Università degli Studi di Cagliari, Monserrato I-09042, Italy.
Email: saba@unica.it; alessio.filippetti@dsf.unica.it

Funding information
MIUR; Fondazione di Sardegna; Università degli Studi di Cagliari; Regione Autonoma della Sardegna

Abstract

Lead-free $Cs_2AgInCl_6$ and $Cs_2AgInBr_6$ double perovskites are studied by a combination of advanced ab-initio calculations and photoluminescence experiments. We show that they are insulators with direct band gaps of 2.53 and 1.17 eV, respectively; most importantly, they are characterized by unusually low absorption rates in a ~1 eV wide energy region above the band gap, caused by rather peculiar electronic properties. Consequently, this low absorption conveys very long recombination lifetimes, up to milliseconds at low temperature. Our theoretical analysis suggests that such materials can achieve a good compromise between photoconversion efficiency (above 10%) and visible transmittance (above 30%), which makes them potentially suited for lead-free semitransparent solar cell applications.

KEYWORDS

hybrid perovskites, lead-free, optical properties

1 | INTRODUCTION

The replacement of the harmful lead (Pb) in lead halide perovskites for efficient, yet low cost solar cells and LEDs[1-5] is one of the most pressing issues in todays' materials science. In fact, solar cells and visible light LEDs based on lead halide perovskites have nowadays reached 25% and more efficiency,[6-15] and outdoor operational capability[2,16-21] is currently tested in view of near-future industrial production and commercialization. However, the presence of toxic, heavy metal Pb gives rise to serious environmental issues, from the contamination of ground water to the treatment of waste storage, whose cost may completely overthrow the economic convenience and sustainability of these systems.[22-26] Alas, lead-free alternatives are all but trivial to envision and realize, owed to the instrumental role played by the Pb electronic properties in several crucial aspects of the photoconversion process, such as the favorable band-gap amplitude and the sizeable orbital extension and bandwidth, in turn favoring high electron mobility and diffusion length, as well as low carrier recombination with trapping defects.

A massive effort was headed toward the simultaneous substitution of Pb, A-site cation and/or anion; however, combinations including a single B-site replacement capable to preserve the abovementioned virtues of lead perovskites remained elusive so far (promising exceptions are Sn-based perovskites[27-44] for solar cells and Ge-based layered perovskites[45-50] for LEDs).

Eventually, what a single cation cannot achieve, can be done, perhaps, by the cooperation of two: this is the

idea which pushed several groups[51-74] to explore the coexistence of two different B-site cations in the same compound, thus extending the chemical template of the search from that of single perovskites to the double perovskites of the form $A_2BB'X_6$; in fact, if B and B′ are not too different and size-compatible with A and X, these materials can grow structurally ordered and highly symmetric, with B and B′ alternating in regular patterns; clearly, the chemical equivalence with Pb^{2+} requires a B^{1+} and B'^{3+} combination.

References 69, 70, and 72 provide useful overviews of the literature concerning both actually synthesized and theoretically simulated halide double perovskites; it is remarkable that many of them adopt the cubic *Fm3m* symmetry,[69] as a consequence of the regular alternation of B and B′ along the three Cartesian directions (so called "G-type" order); this signals an improved thermodynamic stability with respect to the Pb-based prototypes, also favored by the presence of an atomic cation, in place of the molecule, at the A-site; the great potential of these systems is also apparent by the wide variety of band gaps allowed by the presence of two B-site cations, spanning all the useful range for photovoltaic and optical applications. However, having the correct band gap is only a necessary precondition: good amount of the examined double perovskites are found having indirect band gaps[65] and/or absorption spectra smothered by symmetry-forbidden inter-band transitions.[66,68,70] It further complicates the situation the fact that reported data on optical properties for the same materials are spread over a wide range of values, sometime even conflicting with each other; in fact, the variety of growth processing protocols on the experimental side, and of the applied methodologies on the theoretical side, complicates the convergence toward a consistent, unbiased description of these systems. It must be emphasized, in fact, that perovskites are, from a fundamental viewpoint, "complicated" materials, with fairly correlated 3*d* or 4*d* transition-metal electronic states which coexist with highly dispersed *s* and *p* electrons; these cases are not satisfactorily treated by standard local density functional theory (DFT); furthermore, when spin-orbit coupling is small, the fortuitous cancellation occurring in Pb-based perovskites between spin-orbit and correlation effects cannot occur.

This lack of cancellation makes DFT not appropriate for these systems, which require, instead, the use of advanced approaches, smart enough to efficiently combine accuracy of results and computational feasibility. To the aim, our method of choice for this work is the variational pseudo-self-interaction correction (VPSIC),[75] which over the years has demonstrated excellence performances for the description of a vast range of inorganic perovskites, from magnetic to ferroelectric, from superconductive to topological, either in form of bulk systems or low-dimensional heterostructures. In terms of comparison with other popular approaches, the VPSIC ranks at the same accuracy level of the hybrid heyd-scuseria-ernzerhof (HSE) functional (see, for example, Reference 76 and the G_0W_0 approach,[77] albeit requiring a considerably reduced computing workload.

In this work, we focus on two particularly interesting double perovskites, featuring the Ag/In combination at the B site, namely $Cs_2AgInCl_6$ (CAIC) and $Cs_2AgInBr_6$ (CAIB); they can be seen as the reference end-points of a mixed CAI (C/B) series which encompasses a range of uncommon fundamental properties, and have the potential to become the building blocks of a novel stream of lead-free photovoltaic and nanophotonic applications. Specifically, CAIC was recently put in the spotlight by its reportedly efficient warm-white light emission.[67] This compound is characterized by a direct band gap, and quite peculiar absorption and photoluminescence properties which, despite several studies already present in literature,[61-68] are in our opinion not yet well clarified, thus leaving room to substantial uncertainties and speculations; it is sufficient to say that band gap values ranging from 1 to 3.67 eV were reported, according to the specific type of calculation. Here, we present a combined theoretical and experimental study headed to recast in a solid framework the most fundamental aspects of this material. On the other hand, CAIB is much less explored than its Cl-based counterpart.[61,64,74] While difficult to synthesize, being on the verge of a thermodynamic instability, our calculations reveal a system with great potential as a lead-free photovoltaic absorber, with direct band-gap of 1.17 eV and large conversion efficiency. Furthermore, owed to their peculiar absorption spectrum, both CAIC and CAIB display large visible transmission, which makes them potentially exploitable for transparent and semitransparent solar cell windows.

2 | RESULTS AND DISCUSSION

2.1 | Structural properties

In order to determine the equilibrium structure of CAIC and CAIB, extensive energy minimizations were performed, exploring both orthorhombic and rhombohedral symmetries, and fully relaxing cell parameters and internal atomic positions without any imposed space group symmetry, At the end of the optimization process, for both compounds the cubic *Fm3m* symmetry was identified as the ground state. In Figure 1A, the $\sqrt{2}\times\sqrt{2}\times 2$ unit cell is shown. The X-ray powder diffraction pattern of CAIC, refined by the Rietveld method in space group $Fm\bar{3}m$, is shown in Figure 1B. The refinement was

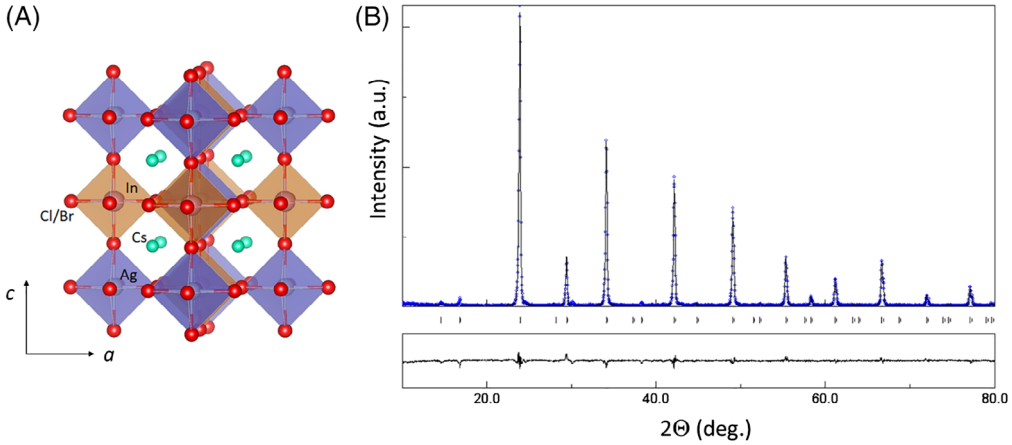

FIGURE 1 A, The $\sqrt{2}\times\sqrt{2}\times 2$ tetragonal unit cell of $Cs_2AgInCl_6$ (CAIC) and $Cs_2AgInBr_6$ (CAIB) double perovskites in cubic *Fm3m* symmetry (space group 225). Axes *a* and *c* refers to the [110] and [001] directions of the cubic cell, respectively. B, Rietveld refined X-ray powder diffraction pattern of CAIC. Lattice parameter $a = 10.4796(5)$ Å, R_{wp} (%) = 12.40, R_B (%) = 10.05, R_{exp} (%) = 11.51, and GOF = 1.04

TABLE 1 Calculated lattice parameter and interatomic distances for $Cs_2AgInCl_6$ (CAIC) and $Cs_2AgInBr_6$ (CAIB) in their cubic *Fm3m* ground-state structure (in parenthesis the available experimental data); *a* is the cubic edge of the 2 × 2 × 2 cell; *Ag-X* and *In-X* are cation anion distances (X = Cl or Br)

	$Cs_2AgInCl_6$	$Cs_2AgInBr_6$
a (Å)	10.39 (10.48)	10.93 (11.0)
Ag-X (Å)	2.661	2.736
In-X (Å)	2.535	2.677

carried out by the software MAUD.[78] The calculated profile agrees very well with the one obtained from the file 1 546 186.CIF reported in Reference 65. The refined lattice parameter is $a = 10.4796(5)$ Å (where *a* is twice the cube edge), in excellent agreement with a previous measurement of 10.47 Å.[61] The calculated lattices are $a = 10.39$ Å for CAIC and $a = 10.93$ Å for CAIB, which compares very well with value 11.0 Å found by XRD.[74] In passing, we remark the striking difference with the cubic-equivalent $a \sim 12.5$ Å of the methylammonium lead iodide prototype, mostly due to the replacement of the molecular sublattice. This much increased structural packing is fingerprint of the higher thermodynamic stability of the double perovskites. The Ag and In atoms are G-type ordered, while the surrounding Cl_6/Br_6 ions undergo a breathing displacement in order to be closer to In than to Ag (see Table 1), as a consequence of the slightly larger ionic radius of the latter (1.6 Å for Ag and 1.55 Å for In).

2.2 | Electronic properties

The electronic properties of CAIC and CAIB are reported in Figure 2, calculated in the $\sqrt{2}\times\sqrt{2}\times 2$ unit cell. The qualitative similarity of the two compounds is apparent: both are characterized by a direct band-gap at the Γ point; however, the valence band top (VPT) is so flat along the cubic directions (Γ-*Z* and Γ-*L*) that indirect transitions are practically degenerate with the direct one. The orbital composition of the bands can be inferred in the orbital-resolved DOS: the valence bands are dominated by the fully occupied Ag *4d* and anion *p* states (Cl *3p* or Br *4p*), while In states are substantially absent in the valence. Owed to the spatially localized nature of the *4d* orbitals, some of the valence states at the VBT are very flat; this specifically concerns the Ag t_{2g} triplet orbitals that do not point toward the anions, and the anion $p_\perp$ orbital doublet (orthogonal to the ligand orbital p_L) that also does not overlap with the cation orbitals. To the point, it is worthy noticing the importance of the cubic symmetry: while octahedral tilting and rotations occurring in lower symmetries always favor orbital mixing, here ligand and orthogonal states remain visibly well distinct in space and energy. The lowest conduction band, on the other hand, is widely dispersed, with bandwidth of 2.2 eV in CAIC and 2.6 eV in CAIB; furthermore, conduction is almost exclusively contributed by In *5s* states, with a very minor contribution from Ag *5s*. The DOS analysis indicates that inter-band absorption is made of transitions from anion p_L to In *5s* states; on the other hand, the Ag sublattice contribution is very minor, since direct transitions from Ag *4d* to In *5s* states are severely suppressed by two factors: *i)* the small spatial overlap of the corresponding orbitals, and *ii)* the parity of both states, which accounts to zero dipole matrix element at the Γ point. We will go back to this important aspect when discussing the optical properties.

It is crucial at this point to discuss the controversial value of the band gap for CAIC, since the range of

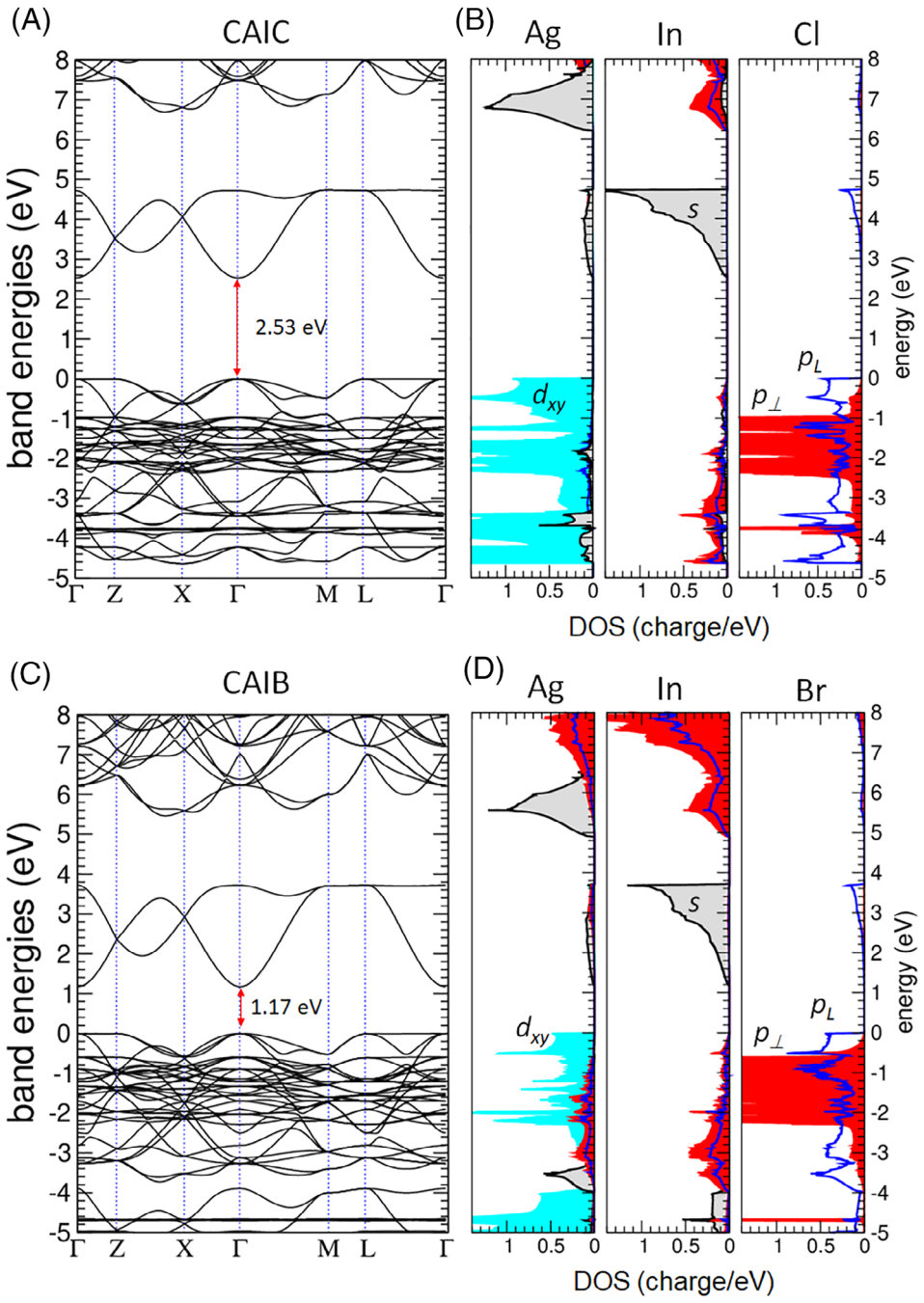

FIGURE 2 A and C, Band structure calculated for $Cs_2AgInCl_6$ (CAIC) and $Cs_2AgInBr_6$ (CAIB), respectively, along several *k*-space, high-symmetry directions of the $\sqrt{2}\times\sqrt{2}\times2$ unit cell; *k*-points are, in crystal coordinates, Z = (0,0,1/2), X = (1/2,0,0), M = (1/2,1/2,1/2), and L = (1/2,1/2,0). B and D, The corresponding atom- and orbital-resolved DOS. Each panel refers to a specific atomic type, indicated in the figure. For each atomic type, only the most important orbitals are shown: *s* (grey), p_L (blue), $p_\perp$ (red), and p_z (green)

calculated values reported in literature is unusually scattered. This uncertainty is partially caused by the various non-standard methodologies employed to the aim, and partially alimented, in our opinion, by the attempt to adhere to what is suggested by experiments which measure the absorption onset for CAIC at large energies ~3.2 to 3.3 eV.[61,63,67] To avoid a misleading scenario, it is important to pinpoint that the band gap of CAIC calculated by standard ab-initio local DFT (LDA) is ~1.0 eV and the LDA underestimate for inorganic, non-magnetic insulators is not larger than 50% to 60%. Thus, whatever the method used to correct the LDA failure, no reasonable way exists to reconcile the calculated band gap and the measured absorption onset. The interpretation outcoming from our results is that, in fact, the absorption threshold does not represent the actual band gap of the system. Our VPISC calculations give E_g = 2.53 eV for CAIC, and 1.17 for CAIB, in agreement with the values delivered by standard HSE.[61,62] It is worthy to keep in mind that these are, as customary for ab-initio band structure, zero-temperature values. In Section 2.4, we demonstrate that temperature effects are large, as evidenced by temperature-dependent photoluminescence measurements for CAIC. Finally, spin-orbit

coupling (not included in the band structures shown in Figure 2) has no visible effect on this scale for the considered materials, in agreement with what is reported in Reference 61; in fact, spin-orbit vanishes for the In *4s* conduction band, and is minor for the Ag *4d* states at the VPT. This marks a huge difference with respect to lead-based perovskites, where the equally large and opposite in sign spin-orbit and correlation effects on the band structure are fortuitously cancelled.

2.3 | Optical properties

We start the analysis from the measured absorption properties of CAIC, for which several terms of comparison are available in literature. UV-Vis Diffuse Reflectance Spectroscopy (UV-Vis-DRS) measurements were performed in a spectrophotometer equipped with integrating sphere. Absorbance spectra were extracted through the Kubelka-Munk function $F(R) = \alpha = (1\text{-}R)^2/2R$, and reported in Figure 3. The Tauc plot $(h\nu F(R))^{1/n}$ vs $h\nu$ ($n = 1/2$ for direct transition) is used to extract the optical bandgap value. The fit gives a direct band gap of 3.53 eV, in agreement with previous values of 3.23,[63] 3.3,[61] and 3.53 eV.[65]

The calculated absorption spectra and refraction indices of CAIC and CAIB are shown in Figure 4. For both materials the absorption presents a wide plateau, extended between the calculated band gap energies (indicated by the vertical black dashed lines), and the steeply rising absorption threshold located about 1 eV above the band gaps. An enlargement of the threshold region is reported in the insets of Figure 4A,B; here, for the sake of comparison with the experiment, a straight green dashed line is juxtaposed to the absorption shoulder, intersecting the energy threshold corresponding to zero absorption. We obtain for CAIC an "optical gap" of 3.66 eV, thus only a bit larger than the value extracted by Tauc plot. For CAIB the same procedure gives 2.1 eV, in satisfying agreement with the 2.36 eV value extracted from Tauc in Reference 74. According to calculations, absorption is small but not vanishing below these energy thresholds: at the plateau, just below the threshold, we calculate absorption rates equal to ~1.5×10^3 cm^{-1} and 5×10^3 cm^{-1} for CAIC and CAIB, respectively, thus, about two order of magnitude smaller than, for example, the $CH_3NH_3PbI_3$ (MAPI) absorption at the band gap edge. Above the threshold the absorption rises steeply, recovering values similar to MAPI after a further energy rising of about 1 eV. The same regime change, indicated by vertical dashed lines, is also well apparent in the calculated refraction spectra (Figure 4C,D), where pronounced peaks appear in correspondence of the threshold.

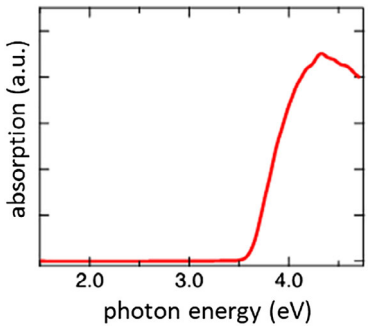

FIGURE 3 Absorption (Kubelka-Munk function $\alpha/s = (1\text{-}R)^2/2R$) vs energy measured at room temperature for $Cs_2AgInCl_6$ (CAIC)

The highly suppressed absorption in the plateau region can be not only consequence of symmetry-forbidden transitions at the band edge as described in previous works,[66,70] but also of strong charge localization: in fact, inter-band transitions between states characterized by highly localized orbitals can be naturally suppressed by their limited overlap. Coherent with this interpretation are the calculated refraction indices of 1.44 and 1.58 for CAIC and CAIB, respectively, and the electronic dielectric constants $\varepsilon_\infty = 2.08$ and 2.49 for CAIC and CAIB, respectively. These numbers radically differ from, for example, those found for the lead-based prototype MAPI (refraction index ≈2.2-2.4 and ε_∞ ≈5-5.2)[79,80] and attest the strong impact of charge localization on the electronic properties of these systems. In fact, while for covalent semiconductors the dielectric constant is roughly proportional to the inverse square root of the energy gap (according to the empirical Moss relation), for transition metals systems strong electron correlation may coexist with small band gaps (and even metallic behaviour). The Ag-based perovskites are a case in point: the band gap is smaller than in MAPI, and yet, the dielectric constant is reduced to about a half by the presence of the localized Ag *4d* states at the valence bands.

In Reference 67, a strategy to avoid parity cancellation was suggested, based on a partial Ag substitution with Na, and resulting in a large increment of photoluminescence quantum yield; in fact, this is also an effective way to reduce the incidence of localized *4d* states at the VBT. To investigate more in detail the optical threshold which separates low and high absorption regime, in Figure 5, we show the detailed analysis of the band structure around the band gap extrema along the z axis (ie, the [001] direction) of the Brillouin zone. The energy-lowest transitions are sketched by colored vertical arrows, with the indication of the dominant orbital characters contributing to the transition (in Table S1 the quantitative account of the calculated effective masses and the specific orbital contributions can be found). In Figure 6,

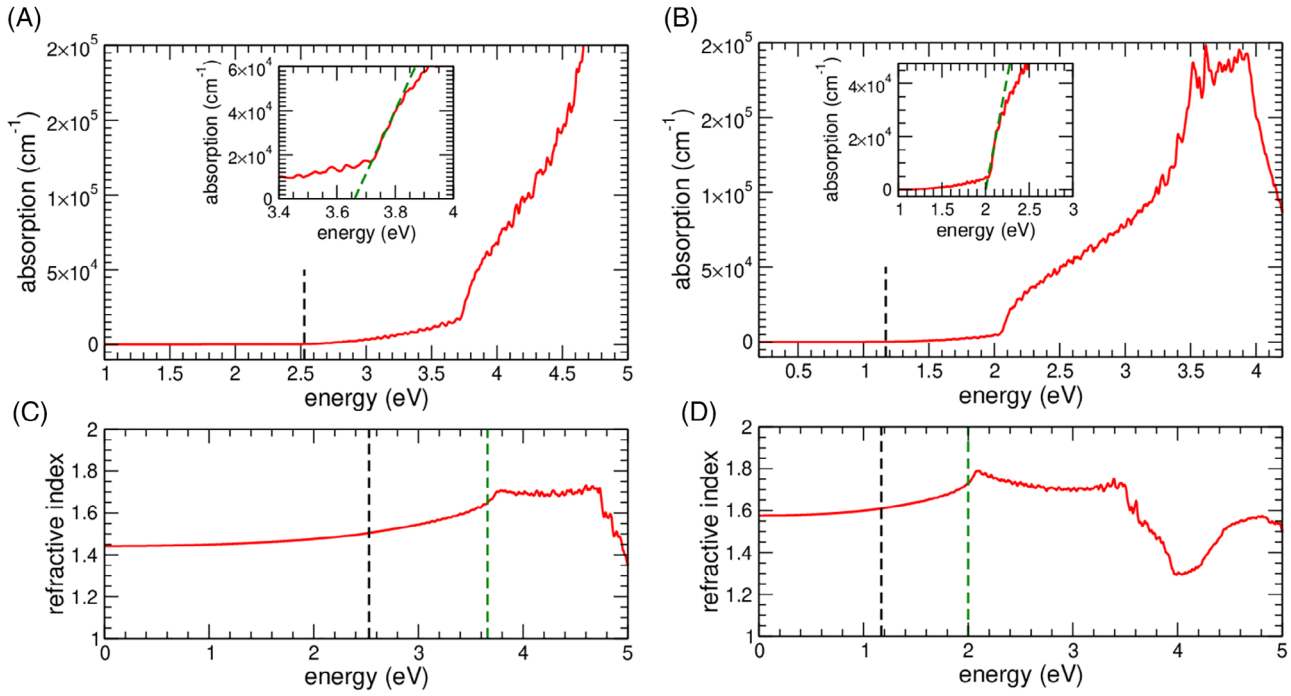

FIGURE 4 A, Calculated absorption spectrum for $Cs_2AgInCl_6$ (CAIC); inset: detail of the threshold region (see text); black and green dashed lines indicate calculated band-gap and optical threshold, respectively. B, The same as (A) for $Cs_2AgInBr_6$ (CAIB). C, Calculated refraction index for CAIC; the dashed lines are the same as in (A) and (B). D, The same as (C) for CAIB

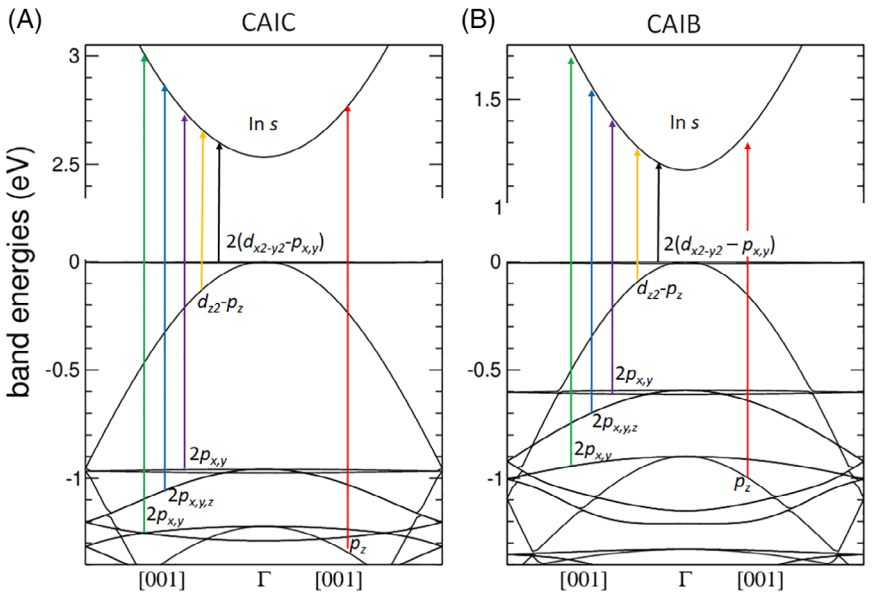

FIGURE 5 Calculated band structures along the k_z axis in a narrow energy window around the band gap; zero energy is fixed at the VBT. The colored arrows identify the energy-lowest inter-band transitions, whose corresponding transition matrix element is reported in Figure 6. The orbital characters are also indicated (*d* states refer to Ag, and *p* states to either Cl or Br)

the relative $|P_x|^2$ (*s*-polarized) and $|P_z|^2$ (*p*-polarized) transition matrix elements are reported, using the same color of the corresponding transition in Figure 5.

At the VBT we find a triplet state at Γ point, which away from Γ splits in a very flat doublet made of Ag d_{x2-y2} and Cl/Br p_x, p_y orbitals, and a dispersed Ag d_{z2} - Cl/Br p_z singlet; the corresponding transitions to the conduction bands are indicated by black and orange arrows, respectively; as can be seen in Figure 6, the former lacks contribution to the absorption at any k, due to the even parity; the dispersed singlet, on the other hand, does contribute to the absorption away from Γ, but only to the z component (the orange curve in Figure 6B). Despite being allowed by symmetry, this contribution is small in amplitude, due to the reduced overlap between In *4s* and d_{z2}-p_z states.

Moving further below in the energy, we encounter another group of four bands: a very flat p_x, p_y doublet

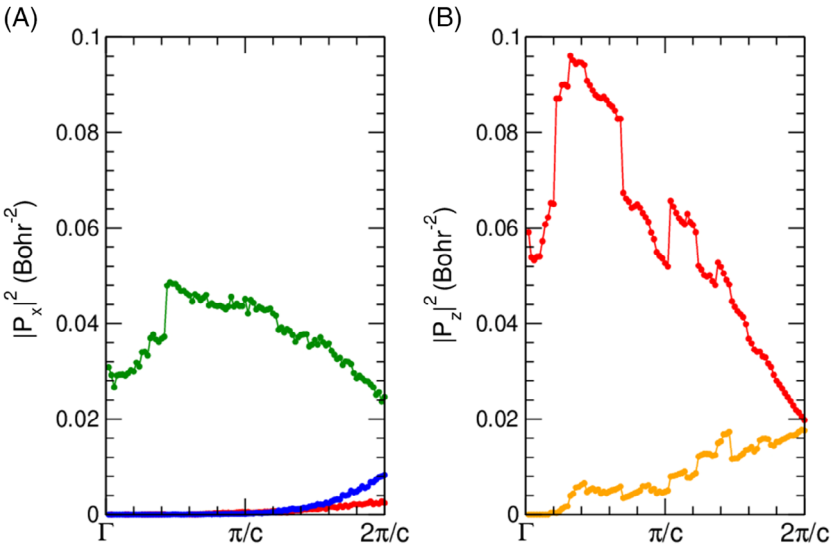

FIGURE 6 Calculated (squared) dipole matrix elements vs k_z for the inter-band transitions drawn with arrows of corresponding color in Figure 5. Matrix elements with $|P|^2 < 10^{-4}$ Bohr are not displayed for clarity and should be assumed vanishing at any k point, by symmetry

(whose transition is indicated by the violet line) and a more dispersed *p*-type hybridized doublet (blue line); the former is completely suppressed by symmetry, while the latter gives a very minor contribution to the *s*-polarized transition near the zone-boundary (the blue curve in Figure 6A. Going further down in energy, we arrive at a Γ-point band triplet which finally activates a substantial absorption; away from Γ, this group splits in a heavy-mass doublet of p_x, p_y character which mostly contribute to the *s*-polarized transition (green line), and a light-mass p_z ligand singlet, whose transition to In *4s* states (red curve) dominates the *p*-polarized absorption. The transition energy from this singlet to the conduction minimum at Γ identifies the "absorption gaps" of 3.53 eV for CAIC, and 2.57 eV for CAIB. The peculiarity of the p_z ligand orbitals resides in the odd parity with respect to the *z*-axis inversion (which avoid matrix cancellation at any *k*-point) and in the orbital spread ($m^* = 0.65$ for CAIC and 0.42 for CAIB, see Table S1) which is sufficiently large to consent a substantial overlap with In *4s* orbitals.

2.4 | Photoluminescence and radiative recombination

The large variety of electronic transitions in these systems leads to a rich and intricate dynamics of carrier recombination, whose detailed account is still lacking, at our knowledge, in present literature. To this aim, we performed time-resolved photoluminescence measurements as a function of temperature, at varying excitation energies and pump power, complemented by ab-initio calculations.

The *PL* spectrum for CAIC (excited at 330 nm wavelength and integrated over the first 5 ns after optical excitation) shown in Figure 7A, is characterized by two distinct features: a sharp UV line at wavelength of 390 nm (3.18 eV), which roughly corresponds to the onset of significant optical absorption, and a broad visible emission, centered around 500 nm (2.48 eV). As the temperature is decreased, the visible emission become more and more intense, at the expenses of the UV emission. The time decay of the two components is also very different (Figure 7B,C): the UV emission is short-lived, with characteristic picosecond lifetimes at all temperatures, while the broadband visible emission lives much longer, with an initial decay in the nanosecond time scale followed by a long, temperature-dependent decay that stretches up to a fraction of ms at 11 K. The linewidth of the visible peak at this low temperature (FWHM ~ 0.4 eV) is substantially reduced with respect to the extra-large (~1 eV) peak found at room temperature.

The double-peaked *PL* fits well the scenario described by VPSIC calculations for CAIC, especially at low temperature: the energy of the visible peak measured at low temperature agrees with the (zero-temperature) calculated band-gap of 2.53 eV, while the high-energy peak can be associated with the calculated optical threshold. Furthermore, the long photoluminescence decay time for the visible emission is coherent with the suppression of band-to-band transitions described in the previous sections. In fact, although the photoemission decay rate is most likely determined by non-radiative processes, the radiative lifetime must be a lower bound of the total, thus long lifetimes necessarily imply very low absorption rates for the visible energy region.

The *PL* decay rates at room temperature, measured at varying excitation wavelengths, are reported in Figure 7D. A rather complicate behavior is put forth: first, the increase of the excitation wavelength from 330 to 360 nm, close to the optical absorption onset, causes the

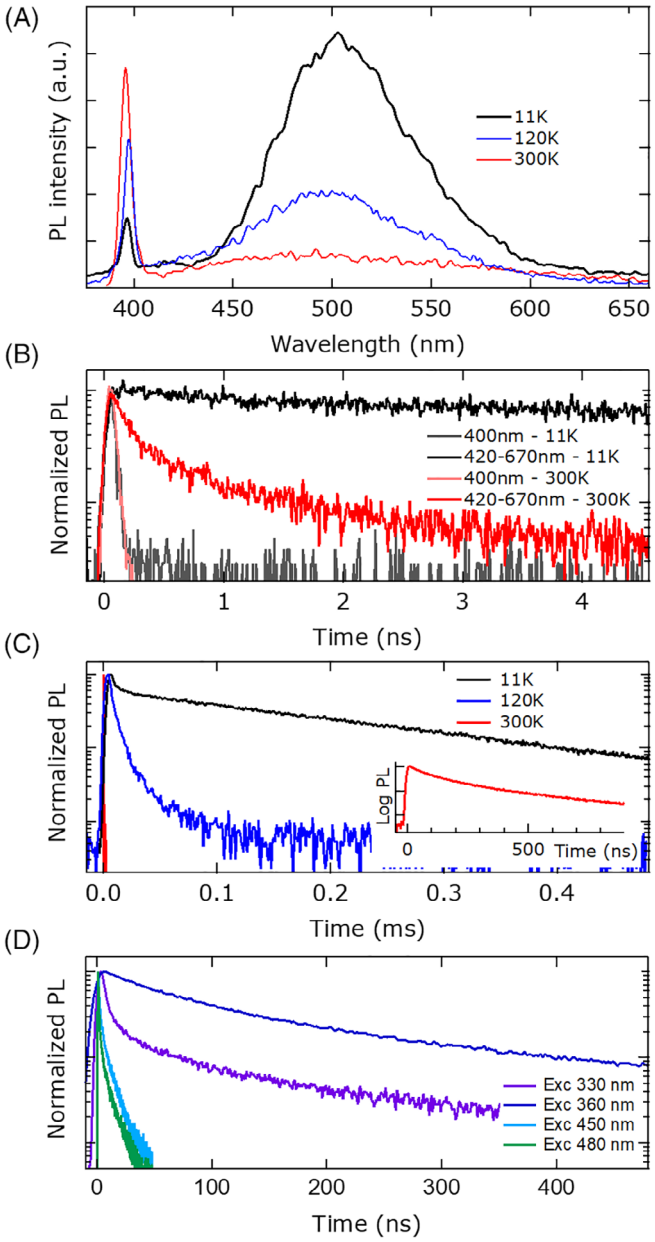

FIGURE 7 A, PL spectrum of $Cs_2AgInCl_6$ (CAIC) for three different temperatures. B, Normalized PL decay rates for two different temperatures, decomposed in UV and visible contributions. C, Normalized decay rate of the PL emitted in the visible spectrum for different temperatures (420-670 nm); the inset displays the decay measured at 300 K on an expanded horizontal axis. D, Normalized PL decay rate at varying excitation energy, measured at room temperature. PL, Photoluminescence

disappearance of the fast component in the *PL* decay. Furthermore, the dynamics change completely for excitations below the optical gap (450 and 480 nm), as the decays became much faster, with characteristic times of a few nanoseconds. This lifetime decrease could be related to the very different optical penetration depth in the visible spectrum with respect to UV (several microns, as opposed to tens of nanometers), causing a different set of crystalline sites to be excited by light; moreover, absorption of visible light may be assisted by defects and preferentially excite sites close to traps, hence the much faster *PL* decay.

While the measured dynamics leaves room to possible interpretations, one aspect of the measurements seems undisputable: the emission of visible light for excitation lower than the absorption onset demonstrates that the true band gap is well below the value inferred from absorption. To this regard, it is worthy to pinpoint out that our description of CAIC is alternative to the scenario proposed in Reference 67, where it is predicted a large band gap of more than 3 eV, and a much lower *PL* emission due to huge (~ eV) contributions from structural-deformation energies and self-trapping excitons; in fact, according to our calculations (described in the Supporting Information) these contributions should not be larger than ~50 meV. Notice also that the free exciton ground-state (whose energy is 0.25 eV according to Reference 67) is symmetry-forbidden, thus it should not contribute to *PL*.

The measured *PL* dynamics does not change as a function of laser fluence, and the overall *PL* intensity scales linearly with excitation intensity. This is compatible with a recombination regime dictated by carrier trapping and/or other non-radiative mechanisms. On the other hand, it is also useful to evaluate the perovskite behavior in the ideal bimolecular limit, since, owed to their peculiar optical properties of these systems, we can expect unusually small recombination rates and extra-long radiative lifetimes. To the aim, we used our ab-initio band structure calculations in combinations with the band-to-band recombination rate calculated according to the Van Roosbroeck-Shockley theory.[81,82] In Figure 8, the recombination properties as a function of the injected electron-hole population n at room temperature are reported.

In the plot of the electron-hole chemical potential, Figure 8A, dashed and dotted straight lines indicate band-gap and large-absorption threshold values; the band gap is crossed at $n_{eh} = 1.5 \times 10^{19}$ cm^{-3} for CAIC, and $n_{eh} = 10^{19}$ cm^{-3} for CAIB; on the other hand, the absorption threshold is reached at $n_{eh} = 1.2 \times 10^{21}$ cm^{-3} for CAIC, and $n_{eh} = 5.2 \times 10^{20}$ cm^{-3} for CAIB. The recombination rate displays a quadratic regime, characterized by linear lifetime and constant B-factor, up to $n = 10^{17}$ cm^{-3} for both materials. In this charge region, the bimolecular coefficients are $B_{rad} = 2.9 \times 10^{-13}$ seconds^{-1} cm^3 and 0.8×10^{-13} seconds^{-1} cm^3 for CAIC and CAIB, respectively, thus about three orders of magnitude lower than in lead-halide perovskites.[79,83-86] Consistently, the radiative lifetimes are three orders of magnitude longer: as a

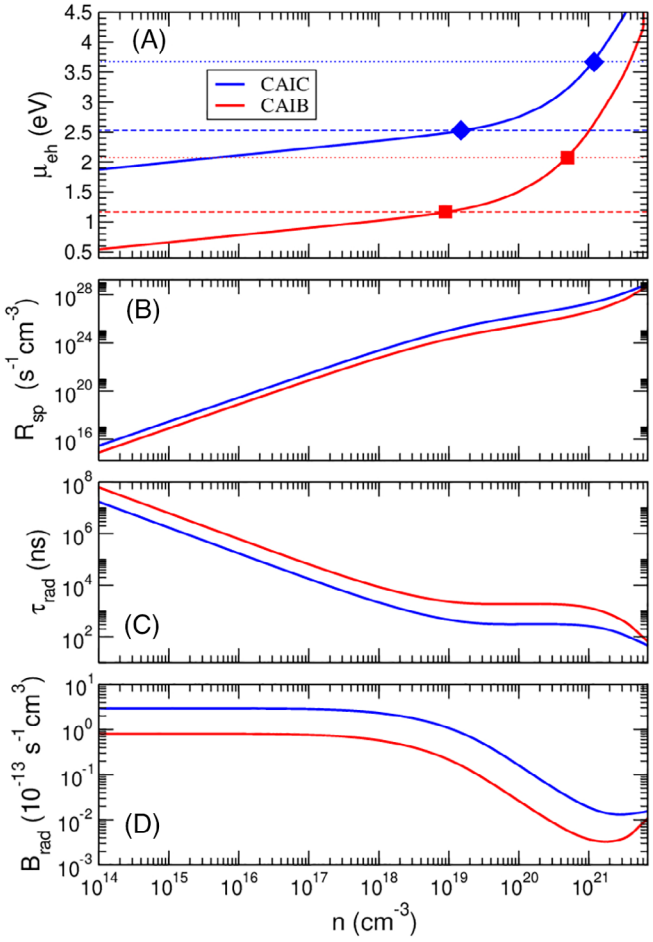

FIGURE 8 Calculated electron-hole chemical potential (μ_{eh}), radiative spontaneous recombination rate (R_{sp}), radiative lifetime (τ_{rad}), and bimolecular coefficient (B_{rad}) as a function of the electron-hole population at room temperature

reference, at $n = 10^{15}$ cm^{-3}, we obtain $\tau_{rad} = 1.5$ and 6 ms for CAIC and CAIB, respectively, in place of the μs order found in MAPI.[86]

This severely reduced recombination is direct consequence of the suppressed inter-band transitions below the optical threshold. Above a charge concentration of $n = 10^{17}$ cm^{-3}, the deviation from the quadratic regime becomes more and more apparent as the density increases; since in our calculations trapping defects and non-radiative mechanisms are not included, these effects are to be attributed to band filling.

2.5 | Conversion efficiency and transparency

In the perspective of using the double perovskites as solar cell absorber, an interesting question concerns how detrimental the small absorption is on the power conversion efficiency (PCE); on the unfavorable side, layer thickness should be largely increased to compensate the reduced absorption rate; on the positive side, the much reduced recombination rate may result in smaller dark current and in turn larger open-circuit bias (V_{oc}). In Figure 9A,B, we display the calculated photocurrent and PCE as a function of applied bias for CAIB, which, due to the favorable band-gap of 1.17 eV, is a potentially suited photo-absorber (details of the method can be found in References 79 and 86, where the same approach was used for MAPI).

Despite the small absorption, short-circuit current densities (J_{sc}) higher than 18 mA/cm^2 can be obtained for reasonably large thickness of $L = 400$ nm, while μm-order thicknesses are required in order to approach J_{sc} values close to their Shockley-Queisser limit. On the other hand, the open-circuit bias is relatively large: the predicted $V_{oc} = 0.99$ eV for $L = 400$ nm corresponds to 85% of the band-gap value, thus, proportionally larger than the same ratio obtained for MAPI.[79] It turns out that the calculated PCE at $L = 400$ nm is 11.3%, ie, a non-disreputable value for a lead-free material. On the other hand, reaching PCE values of 20% and more requires μm-order thickness.

The limited absorption in the visible range suggests a possible application of these systems as transparent or semitransparent solar cells; that is a major research sector of nowadays solar cell technology. The most valuable materials of this kind are those which conjugate satisfying PCE with sufficiently large average visible transmittance (AVT).[87-90] For what concerns hybrid single perovskites, AVT ~22% to 29% associated with 6% to 7% PCE was obtained by reducing the perovskite thickness to less than 40 nm[91]; these values can be improved using perovskites in tandem with silicon and CIGS.[92] However, the need of engineering very thin layers may bring about non trivial processing issues, while having "native" semi-transparency at ordinary thickness would be preferable. To test the potential of our double perovskites to the aim, in Figure 9C, we report the calculated AVT for both CAIB and CAIC, in comparison with the corresponding PCE, as a function of the absorbing thickness. Our results indicate that both systems are quite interesting from this viewpoint: for L~3 to 400 nm, CAIB conjugates a ~10% PCE with a ~30% visible transmission, which ranks among the best semitransparent solar cell performances[88]; for L~100 nm, PCE is reduced to 5%, and the transmission increases to 60%. For CAIC, on the other hand, relatively large PCE (up to a 15% maximum) can only be obtained in the ultrathick limit; however, a μm-thick layer of CAIC can deliver a 5% PCE, and still retain very high (85%) transparency. A simple figure of merit typically used to evaluate the combination of

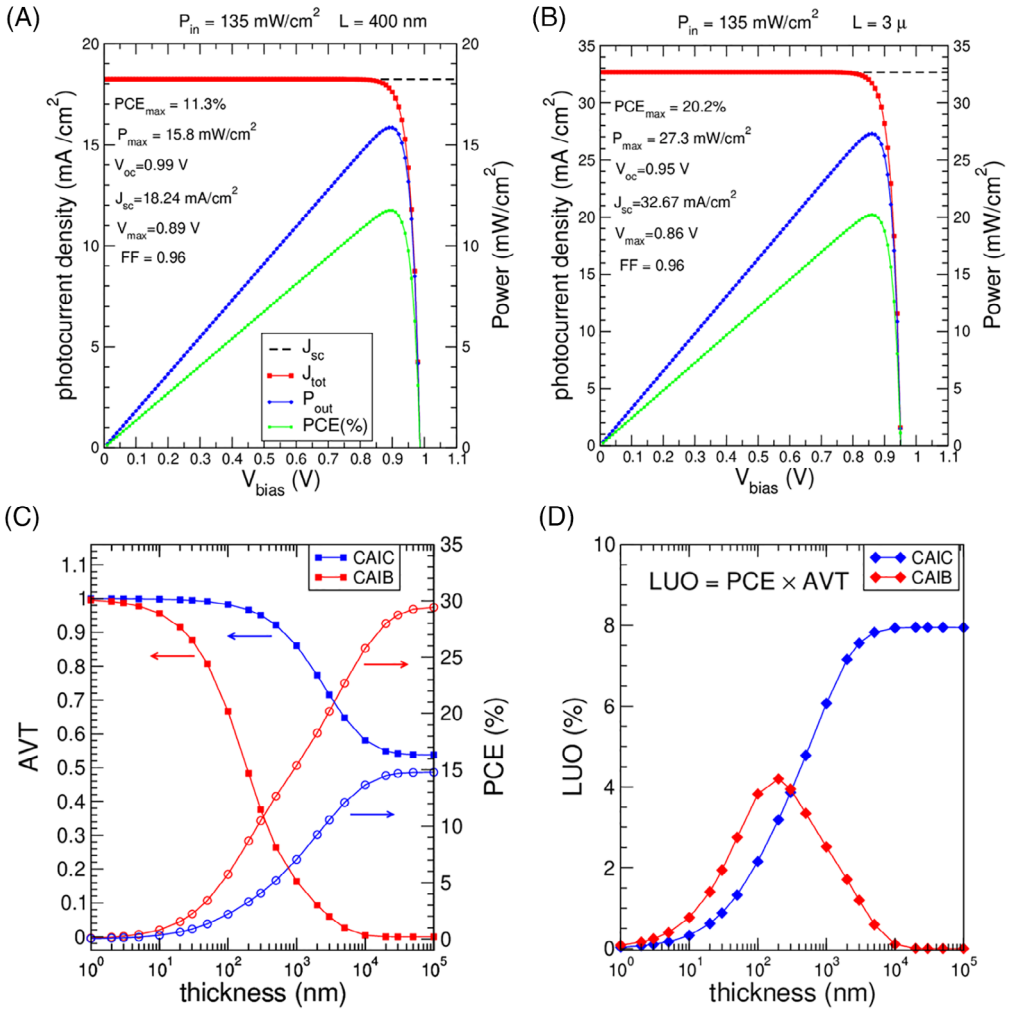

FIGURE 9 A, Calculated short-circuit current density (J_{sc}), total current density (J_{tot}), output power density (P_{out}), and PCE as a function of the applied bias for $Cs_2AgInBr_6$ (CAIB) in the purely band-to-band radiative recombination regime, for a layer thickness $L = 400$ nm. B, The same as (A) but for $L = 3$ μm. C, Calculated AVT and PCE for CAIB (red symbols) and $Cs_2AgInCl_6$ (CAIC) (blue symbols), as a function of layer thickness. D, Calculated LUO for CAIB (red symbols) and CAIC (blue symbols), as a function of layer thickness. AVT, average visible transmittance; LUO, light utilization efficiency; PCE, power conversion efficiency

photoconversion and transparency is the so called light utilization efficiency (LUO),[93] that is, the product of AVT and PCE, reported for the two materials in Figure 9D. We can see that the highest LUO is for CAIB up to a few hundred nanometer thickness, and for CAIC at larger thickness.

3 | CONCLUSIONS

Double perovskites are destined to become one of the major subjects of study in the next few years of materials science. In fact, the flexibility allowed by the presence of two B-site cations lends itself to avoid the malign presence of lead, and hugely extend the search playground of competitive materials in photoconversion and nanophotonic technologies. In this work, we explored two relevant inorganic double perovskites, combining Ag^+ and In^{3+} at the B-site. According to our results, these materials encompass a number of appealing capabilities, from broadband optical emission to potentially large photoconversion efficiency, coupled lo large visible transmission. In particular, we clarified several debated aspects of these systems concerning the band gap amplitude and the photoluminescence dynamics, which stem from the combination of a direct band-gap and a wide energy region with small absorption rate, ultimately due to the specific orbital features of Ag *4d* and In *4s* states. These aspects reflect in bimolecular recombination rates as small as ~10^{-13} seconds^{-1} cm^3, and overlong recombination lifetimes of μm order and more. According to our simulations, these features give rise to a favorable compromise between satisfying conversion efficiencies and large average visible transparency, which make these systems potential candidate for lead-free transparent and semitransparent solar cells.

On the negative side, major faults concern the poor energetic stability of CAIB and, for both materials, a photoconversion performance which even in the bimolecular regime is still substantially distant from that of lead-halide single perovskites. Nevertheless, the flexible configuration of these systems allows a straightforward tuning of the fundamental properties by cation mixing, thus prefiguring large room for improvement. Several strategies of the like

have been already proposed in the literature: for example, the energetic stability of Br-rich compounds can be strengthened by Br/Cl mixing,[61] and the absorption rate can be increased by mixing Ag with other monovalent cations (such as Na[67]) carrying *sp* states in the valence bands. In conclusion, there is strong evidence that these materials possess remarkable potential as starting reference framework for the search of lead-free, highly efficient photo-absorbers and emitters.

Experimental and computational section

Materials preparation: The $Cs_2InAgCl_6$ powder was prepared by precipitation from an acidic solution following the procedure described in Reference 60. In details, 1 mmol of InCl3 (99.999%) and AgCl (99.999%) are first dissolved in 5 mL 10 M HCl. Then 2 mmol of CsCl (99.5%) are added and the solution is heated to 115°C. Immediately after the addition of CsCl, a white precipitate forms and the hot solution is left at 115°C for 30 minutes under gentle stirring to ensure a complete reaction. The solid precipitate is then filtered and washed with ethanol before drying it at low pressure. All the reactants were purchased from Merck-Sigma Aldrich and used without further purification.

X-Ray structural characterization: The X ray diffraction patterns of the polycrystalline samples were recorded on a Siemens D5000 θ-2θ diffractometer, with Cukα radiation and graphite monochromator.

Optical measurements: Diffused optical absorption was measured with a dual-beam spectrophotometer equipped with an integrating sphere accessory (Agilent Technologies Cary 5000 UV-Vis-NIR) under illumination by a nearly collimated light beam and with hemispherical light collection (ϑ/h geometry, ϑ~8°). Photoluminescence (PL) was excited with 100-fs-long laser pulses from a regenerative amplifier (Coherent Libra) pumping an optical parametric amplifier (Light Conversion Topas). Time-resolved PL was then detected with a picosecond streak camera (Hamamatsu) after dispersion in a grating spectrometer (Acton). Samples were kept in vacuum on the cold finger of a closed-circuit cryostat, at a temperature variable between 300 and 11 K.

Ab-initio calculations: For all the analyzed structures, structural optimization was carried out using DFT with generalized-gradient Perdew-Burke-Ernzerhof (GGA-PBEsol) exchange-correlation functional,[94] as implemented in the Quantum Espresso (QE) package,[95] and VPSIC calculations,[75] as implemented in the home-made, freeware PWSIC program (inquiries about the use of the PWSIC code can be addressed to A.F.). All structures were fully relaxed with an atomic force threshold of 10^{-4} Ha/Bohr. Electronic, optical, and recombination properties were all calculated by VPSIC; the VPSIC approach is capable to greatly improve the description of the electronic properties with respect to standard DFT implementations for a vast range of materials characterized by robust electronic correlations, in particular ionic and mixed ionic/covalent insulators.[96-99] Both QE and PWSIC codes are implemented within plane-waves basis functions and ultrasoft pseudopotentials; a plane-wave cut-off energy of 35 Ry was used for all the calculations. Optical properties are calculated starting from the VPSIC band structure; the dielectric function is based on the Drude-Lorentz form, using quasi-particle lifetime of 20 meV. The method was previously applied to the optical properties of MAPI,[79,86] obtaining results in satisfying agreement with the experimental findings. Using the calculated absorption cross section as input, we calculated the band-to-band recombination rate according to the formulation originally proposed by Van Roosbroeck and Shockley, and later generalized by Bhattacharya et al to non-equilibrium conditions (details of the method can be found in Reference 79). Current-voltage and power-voltage curves are calculated in the Shockley-Queisser limit at varying sample thickness L; finally, the calculated transparency $e^{-\alpha L}$ is averaged over the visible energy interval (380-740 nm) to obtain the AVT as a function of L.

ACKNOWLEDGEMENTS

This work was funded by Regione Autonoma della Sardegna through PO-FSE Sardegna 2007-2013, L.R. 7/2007, "Progetti di ricerca di base e orientata," Projects nos. CRP3-114, CRP-17571, CRP-18353, CRP-18013, and CRP-24978, and through Delibera CIPE n. 31 del 20.02.2015 e deliberazione n. 52/36 del 28.10.2015 "Piano Strategico Sulcis," through projects SULCIS-820889 and SULCIS-820947, as well as by MIUR (Italian Ministry of University and Research) through PRIN PERovskite-based Solar cells: toward high Efficiency and lOng-term stability (PERSEO), project id 20155LECAJ. We acknowledge access to research infrastructure in CeSAR - Centro Servizi di Ateneo per la Ricerca - at the Università degli Studi di Cagliari and thank Dr. M. Marceddu for technical assistance. Computational support is acknowledged from CINECA through ISCRA initiative (projects UNWRAPIT and MITOMASC), from PRACE for awarding access to Marconi KNL at CINECA (project DECONVOLVES), and from CRS4 Computing Center (Loc. Piscina Manna, Pula, Italy). A. F. thanks "Progetti biennali d'Ateneo Finanziati dalla Fondazione di Sardegna 2017" (project n. F71I17000170002), and Project PRIN 2017 "TOPSPIN," funded by Italian Ministry of University and Research (MIUR). A.M. and C.C. acknowledge MIUR for funding through project PON04a2_00490 M2M Netergit.

ORCID

Alessio Filippetti https://orcid.org/0000-0002-9144-7005

REFERENCES

1. Correa-Baena J-P, Saliba M, Buonassis T, et al. Promises and challenges of perovskite solar cells. *Science*. 2017;358:739-744.
2. Eperon GE, Hörantner MT, Snaith HJ. Metal halide perovskite tandem and multiple-junction photovoltaics. *Nature Rev Chem*. 2017;1:0095.
3. Green MA, Ho-Baillie A, Snaith HJ. The emergence of perovskite solar cells. *Nature Photon*. 2014;8:506-514.
4. Seok SI, Grätzel M, Park N-G. Methodologies toward highly efficient perovskite solar cells. *Small*. 2018;131:1704177.
5. Snaith HJ. Present status and future prospects of perovskite photovoltaics. *Nature Mater*. 2018;17:372-376.
6. Zhao B, Bai S, Kim V, et al. High-efficiency perovskite–polymer bulk heterostructure light-emitting diodes. *Nature Photon*. 2018;12:783-789.
7. Lin K, Xing J, Quan LN, et al. Perovskite light-emitting diodes with external quantum efficiency exceeding 20 per cent. *Nature*. 2018;562:245-248.
8. Ban M, Zou Y, Rivett JPH, et al. Solution-processed perovskite light emitting diodes with efficiency exceeding 15% through additive-controlled nanostructure tailoring. *Nat Commun*. 2018;9:3892.
9. Cho H, Kim JS, Wolf C, et al. High-efficiency polycrystalline perovskite light-emitting diodes based on mixed cations. *ACS Nano*. 2018;12:2883-2892.
10. Liu X-K, Gao F. Organic–inorganic hybrid Ruddlesden–popper perovskites: an emerging paradigm for high-performance light-emitting diodes. *J Phys Chem Lett*. 2018;9:2251-2258.
11. Zou W, Li R, Zhang S, et al. Minimising efficiency roll-off in high-brightness perovskite light-emitting diodes. *Nat Commun*. 2018;9:608.
12. Yang X, Zhang X, Deng J, et al. Efficient green light-emitting diodes based on quasi-two-dimensional composition and phase engineered perovskite with surface passivation. *Nat Commun*. 2018;9:570.
13. Giuri A, Yuan Z, Miao Y, et al. Ultra-bright near-infrared perovskite light-emitting diodes with reduced efficiency roll-off. *Sci Rep*. 2018;8:15496.
14. Yuan ML, Quan LN, Comin R, et al. Perovskite energy funnels for efficient light-emitting diodes. *Nature Nanotech*. 2016;11:872-877.
15. H.Cho H, Jeong S-H, Park M-H, et al. Overcoming the electroluminescence efficiency limitations of perovskite light-emitting diodes. *Science*. 2015;350:1222-1225.
16. Bruening K, Dou B, Simonaitis J, Lin Y-Y, van Hest MFAM, Tassone CJ. Scalable fabrication of perovskite solar cells to meet climate targets. *Aust Dent J*. 2018;2:2464-2476.
17. Rong Y, Hu Y, Mei A, et al. Challenges for commercializing perovskite solar cells. *Science*. 2018;361:eaat8235.
18. Li Z, Klein TR, Kim DH, et al. Scalable fabrication of perovskite solar cells. *Nat Rev Mater*. 2018;3:18017.
19. Berry JJ, van de Lagemaat J, Al-Jassim JMM, Kurtz S, Yan Y, Zhu K. Perovskite photovoltaics: the path to a printable terawatt-scale technology. *ACS Energy Lett*. 2017;2(11):2540-2544.
20. Park N-G, Grätzel M, Miyasaka MT, Zhu K, Emery K. Toward stable and commercially available perovskite solar cells. *Nat Energy*. 2016;1:16152.
21. Snaith HJ, Lilliu S. The path to perovskite on silicon PV. *SciVPro*. 2018;1:1-8. https://doi.org/10.32386/scivpro.000004.
22. Abate A. Perovskite solar cells go lead free. *Aust Dent J*. 2017;1:659-664.
23. Babayigit A, Ethirajan A, Muller AM, Conings B. Toxicity of organometal halide perovskite solar cells. *Nature Mater*. 2016;15:247-251.
24. Ibn-Mohammed T, Koh SCL, Reaney IM, et al. Perovskite solar cells: an integrated hybrid lifecycle assessment and review in comparison with other photovoltaic technologies. *Renew Sust Energ Rev*. 2017;80:1321-1344.
25. Celik I, Phillips AB, Song Z, et al. Environmental analysis of perovskites and other relevant solar cell technologies in a tandem configuration. *Energy Environ Sci*. 2017;10:1874-1884.
26. Ju M-G, Chen M, Zhou Y, et al. Toward eco-friendly and stable perovskite materials for photovoltaics. *Aust Dent J*. 2018;2:1231-1241.
27. Serrano-Lujan L, Espinosa N, Larsen-Olsen TT, Abad J, Urbina A, Krebs FC. Tin-and lead-based perovskite solar cells under scrutiny: an environmental perspective. *Adv Energy Mater*. 2015;5:1501119.
28. Liu X, Yan K, Tan D, Liang X, Zhang H, Huang W. Solvent engineering improves efficiency of lead-free tin-based hybrid perovskite solar cells beyond 9%. *ACS Energy Lett*. 2018;3:2701-2707.
29. Ke W, Stoumpos CC, Kanatzidis MG. "Unleaded" perovskites: status quo and future prospects of tin-based perovskite solar cells. *Adv Mater*. 2019;31:1803230.
30. Cheng P, Wu T, Liu J, Deng W-Q, Han K. Lead-free, two-dimensional mixed germanium and tin perovskites. *J Phys Chem Lett*. 2018;9:2518-2522.
31. Ito N, Kamarudin MA, Hirotani D, et al. Mixed Sn-Ge perovskite for enhanced perovskite solar cell performance in air. *J Phys Chem Lett*. 2018;9:1682-1688.
32. Nagane S, Ghosh D, Hoye RLZ, et al. Lead-free perovskite semiconductors based on germanium–tin solid solutions: structural and optoelectronic properties. *J Phys Chem C*. 2018;122:5940-5947.
33. Shao S, Liu J, Portale G, et al. Highly reproducible Sn-based hybrid perovskite solar cells with 9% efficiency. *Adv Energy Mater*. 2018;8:1702019.
34. Rajendra Kumar G, Kim H-J, Karupannan S, Prabakar K. Interplay between iodide and tin vacancies in CsSnI3 perovskite solar cells. *J Phys Chem C*. 2017;121:16447-16453.
35. Handa T, Yamada T, Kubota H, Ise S, Miyamoto Y, Kanemitsu Y. Photocarrier recombination and injection dynamics in long-term stable lead-free CH3NH3SnI3 perovskite thin films and solar cells. *J Phys Chem C*. 2017;121:16158-16165.
36. Zhou C, Tian Y, Wang M, et al. Low-dimensional organic tin bromide perovskites and their Photoinduced structural transformation. *Angew Chem Int Ed*. 2017;56:9018-9022.
37. Zhao Z, Gu F, Li Y, et al. Mixed-organic-cation tin iodide for lead-free perovskite solar cells with an efficiency of 8.12%. *Adv Sci*. 2017;4:1700204.
38. Chen L-J, Lee C-L, Chuang Y-J, Wu Z-H, Chen C. Synthesis and optical properties of lead-free cesium tin halide perovskite quantum rods with high-performance solar cell application. *J Phys Chem Lett*. 2016;7:5028-5035.

39. Liao W, Zhao D, Yu Y, et al. Lead-free inverted planar formamidinium tin triiodide perovskite solar cells achieving power conversion efficiencies up to 6.22%. *Adv Mater*. 2016;28:9333-9340.
40. Hao F, Stoumpos CC, Cao DH, Chang RPH, Kanatzidis MG. Lead-free solid-state organic-inorganic halide perovskite solar cells. *Nature Photon*. 2014;8:489-494.
41. Noel NK, Stranks SD, Abate A, et al. Lead-free organic–inorganic tin halide perovskites for photovoltaic applications. *Energy Environ Sci*. 2014;7:3061-3068.
42. Heo JH, Kim J, Kim H, Moon SH, Im SH, Hong K-H. Roles of SnX2 (X = F, cl, Br) additives in tin-based halide perovskites toward highly efficient and stable lead-free perovskite solar cells. *J Phys Chem Lett*. 2018;9:6024-6031.
43. Fang H-H, Adjokatse S, Shao S, Even J, Loi MA. Long-lived hot-carrier light emission and large blue shift in formamidinium tin triiodide perovskites. *Nat Commun*. 2018;9:243.
44. Adjokatse S, Kahmann S, Duim SH, Loi MA. Effects of strontium doping on the morphological, structural, and photophysical properties of FASnI3perovskite thin films. *APL Mater*. 2019;7:031116.
45. Cheng P, Wu T, Zhang J, et al. (C6H5C2H4NH3)2GeI4: a layered two-dimensional perovskite with potential for photovoltaic applications. *J Phys Chem Lett*. 2017;8:4402-4406.
46. Boix PP, Agarwala S, Koh TM, Mathews N, Mhaisalkar SG. Perovskite solar cells: beyond methylammonium lead iodide. *J Phys Chem Lett*. 2015;6:898-907.
47. Kopacic I, Friesenbichler B, Hoefler SF, et al. Enhanced performance of germanium halide perovskite solar cells through compositional engineering. *ACS Appl Energy Mater*. 2018;1:343-347.
48. Krishnamoorthy T, Ding H, Yan C, et al. Lead-free germanium iodide perovskite materials for photovoltaic applications. *J Mater Chem A*. 2015;3:23829-23832.
49. Stoumpos CC, Frazer L, Clark DJ, et al. Hybrid germanium iodide perovskite semiconductors: active lone pairs, structural distortions, direct and indirect energy gaps, and strong nonlinear optical properties. *J Am Chem Soc*. 2015;137:6804-6819.
50. Chang X, Marongiu D, Sarritzu V, et al. Layered germanium hybrid perovskite bromides: insights from experiments and first-principles calculations. *Adv Funct Mater*. 2019;29:1903528.
51. Kamat PV, Bisquert J, Buriak J. Lead-free perovskite solar cells. *ACS Energy Lett*. 2017;2:904-905.
52. Jain A, Voznyy O, Sargent EH. High-throughput screening of lead-free perovskite-like materials for optoelectronic applications. *J Phys Chem C*. 2017;121:7183-7187.
53. Dahl JC, Osowiecki WT, Cai Y, et al. Probing the stability and band gaps of Cs2AgInCl6 and Cs2AgSbCl6 lead-free double perovskite nanocrystals. *Chem Mater*. 2019;31:3134-3143.
54. Filip MR, Hillman S, Haghighirad AA, Snaith HJ, Giustino F. Band gaps of the lead-free halide double perovskites Cs2BiAgCl6 and Cs2BiAgBr6 from theory and experiment. *J Phys Chem Lett*. 2016;7:2579-2585.
55. Pantaler M, Cho KT, Queloz VIE, et al. Hysteresis-free lead-free double-perovskite solar cells by Interface engineering. *ACS Energy Lett*. 2018;3:1781-1786.
56. Zhao X-G, Yang D, Ren J-C, Sun Y, Xiao Z, Zhang L. Rational design of halide double perovskites for optoelectronic applications. *Aust Dent J*. 2018;2:1662-1673.
57. Lee W, Hong S, Kim S. Colloidal synthesis of lead-free silver −indium double-perovskite Cs2AgInCl6 nanocrystals and their doping with lanthanide ions. *J Phys Chem C*. 2019;123:2665-2672.
58. Volonakis G, Filip MR, Haghighirad AA, et al. Lead-free halide double perovskites via heterovalent substitution of noble metals. *J Phys Chem Lett*. 2016;7:1254-1259.
59. McClure ET, Ball MR, Windl W, Woodward PM. Cs2AgBiX6 (X = Br, cl): new visible light absorbing, lead-free halide perovskite semiconductors. *Chem Mater*. 2016;28:1348-1354.
60. Greul E, Petrus ML, Binek A, Docampo P, Bein T. Highly stable, phase pure Cs2AgBiBr6 double perovskite thin films for optoelectronic applications. *J Mater Chem A*. 2017;5:19972-19981.
61. Volonakis G, Haghighirad AA, Milot RL, et al. Cs2InAgCl6: a new lead-free halide double perovskite with direct band gap. *J Phys Chem Lett*. 2017;8:772-778.
62. Xiao Z, Du K-Z, Meng W, Mitzi DB, Yan Y. Chemical origin of the stability difference between copper(I)- and silver(I)-based halide double perovskites. *Angew Chem Int Ed*. 2017;56:12107-12111.
63. Zhou J, Xia Z, Molokeev MS, Zhang X, Peng D, Liu Q. Composition design, optical gap and stability investigations of lead-free halide double perovskite Cs2AgInCl6. *J Mater Chem A*. 2017;5:15031-15037.
64. Zhao X-G, Yang D, Sun Y, et al. Cu−In halide perovskite solar absorbers. *J Am Chem Soc*. 2017;139:6718-6725.
65. Tran TT, Panella JR, Chamorro JR, Morey JR, McQueen TM. Designing indirect–direct bandgap transitions in double perovskites. *Mater Horiz*. 2017;4:688-693.
66. Meng W, Wang X, Xiao Z, Wang J, Mitzi DB, Yan Y. Parity-forbidden transitions and their impact on the optical absorption properties of lead-free metal halide perovskites and double perovskites. *J Phys Chem Lett*. 2017;8:2999-3007.
67. Luo J, Wang X, Li S, et al. Efficient and stable emission of warm-white light from lead-free halide double perovskites. *Nature*. 2018;563:541-545.
68. Luo J, Li S, Wu H, et al. Cs2AgInCl6 double perovskite single crystals: parity forbidden transitions and their application for sensitive and fast UV photodetectors. *ACS Photonics*. 2018;5:398-405.
69. Meyer E, Mutukwa D, Zingwe N, Taziwa R. Lead-free halide double perovskites: a review of the structural, optical, and stability properties as well as their viability to replace lead halide perovskites. *Metals*. 2018;8:667.
70. Li Z, Yin W. Recent progress in Pb-free stable inorganic double halide perovskites. *J Semicond*. 2018;39:071003.
71. Hoye RLZ, Eyre L, Wei F, et al. Fundamental carrier lifetime exceeding 1 μs in Cs2AgBiBr6 double perovskite. *Adv Mater Interfaces*. 2018;5:1800464.
72. Igbari F, Wang Z-K, Liao L-S. Progress of lead-free halide double perovskites. *Adv Energy Mater*. 2019;9:1803150.
73. Roknuzzaman M, Zhang C, Ostrikov K, et al. Electronic and optical properties of lead-free hybrid double perovskites for photovoltaic and optoelectronic applications. *Sci Rep*. 2019;9:718.
74. Breternitz J, Levcenko S, Hempel H, et al. Mechanochemical synthesis of the lead-free double perovskite Cs2[AgIn]Br6 and its optical properties. *J Phys: Energy*. 2019;1:025003.

75. Filippetti A, Pemmaraju CD, Sanvito S, Delugas P, Puggioni D, Fiorentini V. Variational pseudo-self-interaction-corrected density functional approach to the ab initio description of correlated solids and molecules. *Phys Rev B*. 2011;84:195127.
76. Archer T, Pemmaraju CD, Sanvito S, et al. Exchange interactions and magnetic phases of transition metal oxides: benchmarking advanced ab initio methods. *Phys Rev B*. 2011; 84:115114.
77. Matusalem F, Marques M, Teles LK, Filippetti A, Cappellini G. Electronic properties of fluorides by efficient approximated quasiparticle DFT-1/2 and PSIC methods: BaF2, CaF2 and CdF2 as test cases. *J Phys Condens Matter*. 2018;30:365501.
78. Luterotti L. *Acta Cryst*. 2000; A56, s54; Maud: Materials Analysis Using Diffraction, Version 2.33; 2010.
79. Filippetti A, Delugas P, Mattoni A. Radiative recombination and photoconversion of methylammonium lead iodide perovskite by first principles: properties of an inorganic semiconductor within a hybrid body. *J Phys Chem C*. 2014;118:24843-24853.
80. Filippetti A, Mattoni A, Caddeo C, Saba MI, Delugas P. Low electron-polar optical phonon scattering as a fundamental aspect of carrier mobility in methylammonium lead halide CH3NH3PbI3 perovskites. *Phys Chem Chem Phys*. 2016;18: 15352-15362.
81. Van Roosbroeck W, Shockley W. Photon-radiative recombination of electrons and holes in germanium. *Phys Rev*. 1954;94: 1558-1560.
82. Bhattacharya R, Pal B, Bansal B. On conversion of luminescence into absorption and the van Roosbroeck-Shockley relation. *Appl Phys Lett*. 2012;100:222103.
83. D'Innocenzo V, Kandada ARS, De Bastiani M, Gandini M, Petrozza A. Tuning the light emission properties by band gap engineering in hybrid lead halide perovskite. *J Am Chem Soc*. 2014;136:17730-17733.
84. Wehrenfennig C, Eperon CGE, Johnston MB, Snaith HJ, Herz LM. High charge carrier mobilities and lifetimes in organolead trihalide perovskites. *Adv Mater*. 2014;26:1584-1589.
85. Saba M, Cadelano M, Marongiu D, et al. Correlated electron-hole plasma in organometal perovskites. *Nat Commun*. 2014;5: 5049.
86. Filippetti A, Caddeo C, Delugas P, Mattoni A. Photoluminescence, optical gain, and lasing threshold in CH3NH3Pb3 methylammonium lead-halide perovskites by ab initio calculations. *J Mater Chem C*. 2017;5:12758-12768.
87. Treml BE, Hanrath T. Quantitative framework for evaluating semitransparent photovoltaic window. *ACS Energy Lett*. 2016;1: 391-394.
88. Husain AAF, Hasan WZW, Shafie S, Hamidon MN, Pandey SS. A review of transparent solar photovoltaic technologies. *Renew Sust Energ Rev*. 2018;94:779-791.
89. Hu Z, Wang Z, Zhang F. Semitransparent polymer solar cells with 9.06% efficiency and 27.1% average visible transmittance obtained by employing a smart strategy. *J Mater Chem A*. 2019; 7:7025-7032.
90. Marongiu D, Lai S, Sarritzu V, et al. Bifacial diffuse absorptance of semitransparent microstructured perovskite solar cells. *ACS Appl Mater Interfaces*. 2019;11:10021-10027.
91. Roldán-Carmona C, Malinkiewicz O, Betancur R, et al. High efficiency single-junction semitransparent perovskite solar cells. *Energy Environ Sci*. 2014;7:2968-2973.
92. Bailie CD, Christoforo MG, Mailoa JP, et al. Semi-transparent perovskite solar cells for tandems with silicon and CIGS. *Energy Environ Sci*. 2015;8:956-963.
93. Traverse CJ, Pandey R, Barr MC, Lunt RR. Emergence of highly transparent photovoltaics for distributed applications. *Nat Energy*. 2017;2:849-860.
94. Perdew JP, Ruzsinszky A, Csonka GI, et al. Restoring the density-gradient expansion for exchange in solids and surfaces. *Phys Rev Lett*. 2008;100:136406.
95. Giannozzi P, Baroni S, Bonini N, et al. QUANTUM ESPRESSO: a modular and open-source software project for quantum simulations of materials. *J Phys Condens Matter*. 2009;21:395502.
96. Filippetti A, Fiorentini V. Double-exchange driven ferromagnetic metal-paramagnetic insulator transition in Mn-doped CuO. *Phys Rev B*. 2006;74:220401.
97. Puggioni D, Filippetti A, Fiorentini V. Ordering and multiple phase transitions in ultrathin nickelate superlattices. *Phys Rev B*. 2012;86:195132.
98. Delugas P, Filippetti A, Verstraete MJ, Pallecchi I, Marré D, Fiorentini V. Doping-induced dimensional crossover and thermopower burst in Nb-doped SrTiO3 superlattices. *Phys Rev B*. 2013;88:045310.
99. Delugas P, Filippetti A, Gadaleta A, Pallecchi I, Marré D, Fiorentini V. Large band offset as driving force of two-dimensional electron confinement: the case of SrTiO3/SrZrO3 interface. *Phys Rev B*. 2013;88:115304.

SUPPORTING INFORMATION

Additional supporting information may be found online in the Supporting Information section at the end of this article.

How to cite this article: Liu F, Marongiu D, Pau R, et al. Ag/In lead-free double perovskites. *EcoMat*. 2020;2:e12017. https://doi.org/10.1002/eom2.12017